

# JGR Solid Earth

## RESEARCH ARTICLE

10.1029/2021JB022939

### Key Points:

- Thermal ionization of hydrogen occurs from cation sites at high temperature
- The ionized hydrogen leads to enhanced and highly anisotropic proton conductivity
- Hydrogen at the Mg vacancy site is more mobile than hydrogen at the Si vacancy

### Supporting Information:

Supporting Information may be found in the online version of this article.

### Correspondence to:

Y. He,  
[heyu@mail.gyig.ac.cn](mailto:heyu@mail.gyig.ac.cn)





### Citation:

He, Y., Dai, L., Kim, D. Y., Li, H., & Karato, S.-i. (2021). Thermal ionization of hydrogen in hydrous olivine with enhanced and anisotropic conductivity. *Journal of Geophysical Research: Solid Earth*, 126, e2021JB022939. <https://doi.org/10.1029/2021JB022939>

Received 5 AUG 2021

Accepted 5 SEP 2021

# Thermal Ionization of Hydrogen in Hydrous Olivine With Enhanced and Anisotropic Conductivity

Yu He<sup>1,2</sup> , Lidong Dai<sup>1</sup> , Duck Young Kim<sup>2</sup> , Heping Li<sup>1</sup>, and Shun-ichiro Karato<sup>3</sup> 

<sup>1</sup>Key Laboratory of High-Temperature and High-Pressure Study of the Earth's Interior, Institute of Geochemistry, Chinese Academy of Sciences, Guiyang, China, <sup>2</sup>Centre for High Pressure Science and Technology Advanced Research (HPSTAR), Shanghai, China, <sup>3</sup>Department of Geology & Geophysics, Yale University, New Haven, CT, USA

**Abstract** Trace amounts of hydrogen in olivine can significantly increase its conductivity. However, the conduction mechanism in hydrous olivine is still unclear, which hinders the in-depth understanding of the high conductivity structures of the asthenosphere. We investigate the proton conduction mechanism in hydrous olivine using *ab initio* calculations. Several models were examined using climbing image nudged elastic band and *ab initio* molecular dynamics methods. We found that hydrogen trapped at the Mg (or Fe) defect is more mobile than hydrogen trapped at the Si defect. At high temperature, we observed the ionization of hydrogen from cation defects leading to high and anisotropic proton conductivity along the [100] direction. The highly anisotropic conductivity caused by thermal ionized hydrogen at high temperature explains the experimental observations on olivine single crystals.

**Plain Language Summary** Previous experimental studies show that hydrous olivine has higher conductivity than dry olivine, and the conductivity is highly anisotropic. However, the conduction mechanism in hydrous olivine is still under controversy. Density functional theory (DFT) calculation based on quantum mechanics is able to investigate the mechanism in atomic-scale. Therefore, we conducted DFT calculations on several hydrous olivine models with different hydrogen content, iron content, and kinds of hydrogen defects. We observed the ionization of hydrogen to form free protons at high temperature, which is able to diffuse fast in the olivine crystalline leading to high and anisotropic proton conductivity. The calculated conductivity is consistent with experimental studies at high temperature and gives a mechanism for the observed anisotropic conductivity. In addition, we found hydrogen associated with Mg vacancy site is more mobile than hydrogen associated with Si vacancy site. This atomic-scale investigation is beneficial in understanding the experimental results as well as the high conductivity anomalies at the asthenosphere.

## 1. Introduction

Electrical conductivity inferred from electromagnetic induction such as MT (magnetotellurics) provides important constraints on the composition and temperature of Earth's interior. Particularly important question is the causes of high ( $10^{-1}$ – $10^{-2}$  S/m) and highly anisotropic conductivity observed at the top of the oceanic asthenosphere (Baba et al., 2006, 2010; Evans et al., 2005; Heinson et al., 2000; Naif et al., 2013; Sarafian et al., 2015).

These observations have been explained by the presence of partial melting (e.g., Sifré et al., 2014; Yoshino et al., 2006), or by deformation-induced dynamic recrystallization (e.g., Pommier et al., 2018), or by the influence of hydrogen (e.g., Dai & Karato, 2014a; Karato, 1990; Wang et al., 2006). Among these models, problems with partial melting and recrystallization models are discussed by Karato (2019). He presented discussions showing a difficulty with a partial melt model based on the discussions on the amount of melt, and a difficulty of a model invoking small grain-size based on the inferred small stress in the asthenosphere. Therefore, we focus on the hydrogen model in this study.

The role of hydrogen to enhance electrical conductivity of olivine was first proposed by Karato (1990) based on the high diffusion coefficient of hydrogen in olivine (Mackwell & Kohlstedt, 1990). This hypothesis has been tested by several studies (e.g., Dai & Karato, 2014a, 2014b; Fei et al., 2020; Novella et al., 2017; Poe et al., 2010; Sun et al., 2019; Wang et al., 2006; Yang, 2012; Yoshino et al., 2006, 2009). However, these studies demonstrated some challenges including the experimental difficulties such as hydrogen loss or gain

during the conductivity measurements and the complications in the way in which hydrogen contributes to electrical conductivity. Consequently, there remain a few important issues to evaluate the validity of the hydrogen-assisted conductivity model to explain the observed electrical conductivity of the asthenosphere.

The issues on the experimental studies have been reviewed (Karato, 2019; Karato & Wang, 2013). Here, we focus on the issues of microscopic mechanisms of hydrogen-assisted electrical conductivity from theoretical point of view. The idea of hydrogen-assisted conductivity was proposed based on the observed high diffusivity of hydrogen according to the Nernst-Einstein relationship for ionic conductivity,

$$\sigma = \frac{fDCq^2}{kT} \quad (1)$$

where  $\sigma$  is electrical conductivity,  $f$  is a formation factor approximately equal to unity,  $D$  is diffusion coefficient,  $C$  is concentration of charged species whose electric charge is  $q$ ,  $k$  is the Boltzmann constant, and  $T$  is the temperature. When the concentration of hydrogen is fixed, the activation enthalpy of electrical conductivity should agree with that of diffusion, and electrical conductivity should be proportional to the concentration of hydrogen. However, experimental studies (Wang et al., 2006) showed that the activation enthalpy of electrical conductivity is substantially smaller than that of diffusion and that the water content dependence is weaker than a simple model predict  $\sigma \propto C^r$  with  $r < 1$ . Consequently, Wang et al., (2006) proposed that not all dissolved hydrogen contribute to electrical conductivity equally. In particular, Karato (2013, 2015) proposed that hydrogen trapped at M-site may show large anisotropic diffusion (electrical conductivity) while interstitial hydrogen may show nearly isotropic diffusion.

However, there have been no detailed theoretical support for such a model. For example, high anisotropy diffusion of hydrogen trapped at M-site is proposed in analogy with the observed anisotropy on D-H diffusion (Du Frane & Tyburczy, 2012) with the help of a theory of isotopic diffusion in ionic crystals containing multiple isotopic species (Karato, 2013). Consequently, it is important to examine the role of hydrogen in electrical conductivity of olivine in more detail. The main goal of this study is to investigate how hydrogen at different sites migrates in olivine using theoretical calculations of hydrogen migration with the emphasis on the magnitude and anisotropy of diffusion coefficient.

## 2. Hydrogen in Olivine

Hydrogen can be dissolved in olivine through a variety of mechanisms (e.g., Berry et al., 2005; Karato, 2008; Le Losq et al., 2019; Tollan et al., 2017), and at a given thermodynamic condition, hydrogen at various sites should coexist. The relative amount of hydrogen at each site is controlled by the thermodynamic condition and therefore the dominant type of hydrogen (the most abundant hydrogen) will change with thermodynamic conditions. One of the remarkable observations on hydrogen-assisted electrical conductivity in olivine is that conductivity is highly anisotropic at high temperature, while it is nearly isotropic at low temperatures. In addition, activation enthalpy at high temperature is higher than the enthalpy at low temperature (Dai & Karato, 2014a).

Given these backgrounds, we can extend Equation 1 to

$$\sigma = \sum_j \frac{f_j D_j C_j q^2}{kT} \quad (2)$$

where  $q$  is the charge of proton,  $f_j$  is the formation factor for the  $j$ -th species ( $\sim 1$ ),  $D_j$  is diffusion coefficient of the  $j$ -th species, and  $C_j$  is the concentration of the  $j$ -th species. Our focus is  $D_j$  for hydrogen at various sites particularly hydrogen at M- and hydrogen at Si-site. We calculated the magnitude of diffusion coefficient as well as its anisotropy for hydrogen located at M- or Si-site. Among various hydrogen-related species, we consider  $(2H)_M^\times$  and  $(4H)_{Si}^\times$  in this study.

$(2H)_M^\times$  and  $(4H)_{Si}^\times$  are formed in “pure” olivine that does not contain any aliovalent impurities (Umemoto et al., 2011; Verma & Karki, 2009; Walker et al., 2007). However, in natural olivine a few types of aliovalent point defects are present that would affect the concentration of hydrogen-related defects. These aliovalent defects include  $Fe_M^\bullet$  (ferric iron at M-site) and  $Ti_M^{\bullet\bullet}$  ( $Ti^{4+}$  at M-site) (Blanchard et al., 2017; Kohlstedt & Mackwell, 1998; Mackwell & Kohlstedt, 1990; Withers et al., 2011; Zhao et al., 2004). In this study, we also consider hydrogen associated with  $Fe_M^\bullet$  defect.

**Table 1**

The Olivine Models for Ab Initio Molecular Dynamics (AIMD) Simulations With Different Water and Iron Contents (Fe has the Valence of +2 and +3 Shown in the Composition)

Models	Composition	Defects	C <sub>H2O</sub> (ppm wt)	Fe/(Mg + Fe)
Model 1	Mg <sub>30</sub> Si <sub>16</sub> O <sub>64</sub> H <sub>4</sub>	(2H) <sub>Mg</sub> <sup>x</sup>	16,330	0
Model 2	Mg <sub>32</sub> Si <sub>14</sub> O <sub>64</sub> H <sub>8</sub>	(4H) <sub>Si</sub> <sup>x</sup>	32,683	0
Model 3	Mg <sub>28</sub> Fe <sup>3+</sup> <sub>2</sub> Si <sub>16</sub> O <sub>64</sub> H <sub>2</sub>	$\left[ (Fe)_{Mg}^{\bullet} (H)_{Mg}' \right]^x$	7,938	6.67%
Model 4	Mg <sub>31</sub> Si <sub>16</sub> O <sub>64</sub> H <sub>2</sub>	(2H) <sub>Mg</sub> <sup>x</sup>	8,078	0
Model 5	Mg <sub>28</sub> Fe <sup>2+</sup> <sub>3</sub> Si <sub>16</sub> O <sub>64</sub> H <sub>2</sub>	(2H) <sub>Mg</sub> <sup>x</sup>	7,747	9.375%
Model 6	Mg <sub>71</sub> Si <sub>36</sub> O <sub>144</sub> H <sub>2</sub>	(2H) <sub>Mg</sub> <sup>x</sup>	3,570	0
Model 7	Mg <sub>68</sub> Fe <sup>2+</sup> <sub>2</sub> Fe <sup>3+</sup> <sub>2</sub> Si <sub>35</sub> O <sub>144</sub> H <sub>2</sub>	(2H) <sub>Mg</sub> <sup>x</sup>	3,488	5.6%
Model 8	Mg <sub>28</sub> Fe <sup>2+</sup> <sub>2</sub> Fe <sup>3+</sup> Si <sub>16</sub> O <sub>64</sub> H	$\left[ (Fe)_{Mg}^{\bullet} (H)_{Mg}' \right]^x$	3,875	9.375%
Model 9	Mg <sub>57</sub> Fe <sup>2+</sup> <sub>5</sub> Fe <sup>3+</sup> Si <sub>32</sub> O <sub>128</sub> H	$\left[ (Fe)_{Mg}^{\bullet} (H)_{Mg}' \right]^x$	1,928	9.375%

The ionizations of the H-bearing defects produce interstitial protons as:

$$(2H)_M^x = 2H_I^{\bullet} + V_M'' \quad (3)$$

$$(4H)_{Si}^x = 4H_I^{\bullet} + V_{Si}'''' \quad (4)$$

$$\left[ (Fe)_M^{\bullet} (H)_M' \right]^x = H_I^{\bullet} + (Fe)_M^{\bullet} + V_M'' \quad (5)$$

where  $H_I^{\bullet}$  is proton in the interstitial site formed by these ionization reactions. Interstitial protons migrate easily through the crystalline lattice. Therefore, hydrogen-assisted conductivity is determined by the nature of ionization and the mobility of interstitial proton formed by ionization. The climbing image nudged elastic band (CINEB) method (Henkelman et al., 2000) and the *ab initio* Molecular Dynamics (AIMD) simulations based on density functional theory (DFT) were used to investigate proton diffusion behavior at these defects in hydrous olivine at high *P-T*.

### 3. Computational Methods

#### 3.1. Model Construction and Lattice Relaxation

Different models (Model 1 to Model 9) of hydrous olivine were constructed by replacing the relevant atoms from an Mg<sub>2</sub>SiO<sub>4</sub> supercell with hydrogen (Table 1). The structure of Mg<sub>2</sub>SiO<sub>4</sub> has been optimized using the DFT. In the case of (2H)<sub>Mg</sub><sup>x</sup> (Model 1), one Mg atom at metal site 1 was replaced with two hydrogen atoms (Mg<sub>15</sub>Si<sub>8</sub>O<sub>32</sub>H<sub>2</sub>). For (4H)<sub>Si</sub><sup>x</sup> (Model 2), one Si atom was replaced with four hydrogen atoms (Mg<sub>16</sub>Si<sub>7</sub>O<sub>32</sub>H<sub>4</sub>). For  $\left[ (Fe)_{Mg}^{\bullet} (H)_{Mg}' \right]^x$  (Model 3), one proton was added to the V<sub>Mg</sub><sup>''</sup> site, associated with a nearby Fe<sup>3+</sup> in an Mg<sub>2</sub>SiO<sub>4</sub> supercell (Mg<sub>14</sub>FeSi<sub>8</sub>O<sub>32</sub>H). In our calculations, we did not consider the metal sites 2 (M2 site) as the vacancy generation energy at that site is much higher than that of metal site 1 (M1 site) (Brodholt & Refson, 2000; Umemoto et al., 2011). The other models were constructed in the same manner, and all the models satisfy the charge neutrality condition.

We constructed different models to control types of hydrogen defect, water content, and Fe content in hydrous olivine. All the models and their atomic positions were optimized using the DFT method (Kohn & Sham, 1965) within the Generalized Gradient Approximation (Perdew & Zunger, 1981). All computations were carried out using the Vienna *Ab Initio* Simulation Package (Kresse & Furthmüller, 1996). The calcula-

tions included a plane wave representation of the wave function with a cutoff energy of 800 eV. The defects bearing structures with various hydrogen positions at the cation sites were optimized at the hydrostatic condition until all the forces acting on ions were less than 0.01 eV Å<sup>-1</sup> per atom, and the structures with minimized energy were chosen for subsequent calculations. K-point mesh with a spacing of ca. 0.03 Å<sup>-1</sup> was adopted. The details for the Model 1 to Model 9 are listed in Table 1.

### 3.2. Proton Migration Path and Barrier Energy

A proton migrates along various positions including a position where energy of the system has a local saddle point. The energy difference between this configuration and the configuration where all the atoms are in their original positions is the energy barrier for proton migration. Proton migration barrier energies along various high-symmetry directions from one cation vacancy to another nearby cation vacancy were calculated by CINEB method (Henkelman et al., 2000). This CINEB method duplicated a series of images (7 and 11 images in our calculations) between the starting point and the end point of migrating ion to simulate the intermediate states, with the positions of the starting point and the end point fixed. The actual diffusion pathway and migration barrier energy between the starting and the end point are obtained after the optimization. Only the  $\Gamma$  point was adopted for k-point sampling to reduce the computational cost. The convergence check indicates that a denser k-mesh does not affect our conclusion qualitatively. In order to investigate the barrier energies of proton migration from one cation site to another, we generated relatively large supercells for calculations.  $4 \times 1 \times 2$ ,  $2 \times 2 \times 2$ , and  $2 \times 1 \times 2$  supercells were used to calculate the barrier energies along the [100], [010], and [001] directions in Model 1 and Model 3, respectively. For Model 2, larger supercells ( $8 \times 1 \times 2$ ,  $2 \times 4 \times 2$ , and  $2 \times 1 \times 4$ ) with less water contents are adopted for CINEB calculations. A larger supercell  $6 \times 1 \times 3$  (506 atoms) was generated for the study on proton migration property with less water content of 3,570 ppm wt.

### 3.3. Proton Conductivity Calculations

AIMD simulations have been widely used to study elastic properties, ionic conductivity, melting temperature, and viscosity of minerals at high  $P$ - $T$  (Alfè & Gillan, 1998; Belonoshko et al., 2009; Mookherjee et al., 2008). Here, we use AIMD to calculate the proton conductivity in hydrous olivine. The energy cutoff was reduced to 400 eV and Brillouin zone sampling was performed at the  $\Gamma$  point. The convergence has been checked with denser K-mesh and higher cutoff energy (Figure S1). An equilibration step was first carried out in the canonical ensemble (constant  $N$ ,  $V$ ,  $T$ ) using a Nosé thermostat. The model system was thermally equilibrated for 2 ps first, followed by a MD (molecular dynamics) run at different temperatures (1,000–2000 K) for approximately 30 ps. The pressure is about 5 GPa. The calculated volumes of forsterite at elevated temperatures were compared with previous experimental measurements (Anderson & Suzuki, 1983; Downs et al., 1996; Guyot et al., 1996) as shown in Figure S2 and Table S1. The differences are less than 1%. Our recent AIMD study also gives consistency cell parameters comparable to experimental results at high temperatures (He et al., 2021). The stability of the forsterite structure at 5 GPa and 1600 K was also verified using  $NPT$  ensemble (Figure S3). We also analyzed the stress field of our calculation models, and the hydrostatic condition is maintained in our calculations (Figure S4 and Table S2).

The time averaged mean square displacements (MSD) of the different atoms were calculated using the atomic configuration from each finite MD time step, defined as:

$$\langle [\bar{r}(t)]^2 \rangle = \frac{1}{N} \sum_{i=1}^N \langle [\bar{r}_i(t + t_0) - \bar{r}_i(t_0)]^2 \rangle \quad (6)$$

where,  $\bar{r}_i(t)$  is the displacement of the  $i$ th proton at time  $t$ , and  $N$  is the total number of protons in the system. In practice,  $D$  (diffusion coefficient) is obtained by a linear fit to the time dependence of the average MSD,

$$D = \lim_{t \rightarrow \infty} \left[ \frac{1}{2dt} \langle [\bar{r}(t)]^2 \rangle \right] \quad (7)$$

where  $d$  is the dimension of the lattice on which ion hopping takes place. In the calculation of anisotropic diffusion coefficient along the [100], [010], and [001] directions, MSDs along these directions were calculated, and the value  $d$  was set to 1. The obtained  $D$  at various temperatures can be fitted with the Arrhenius equation:

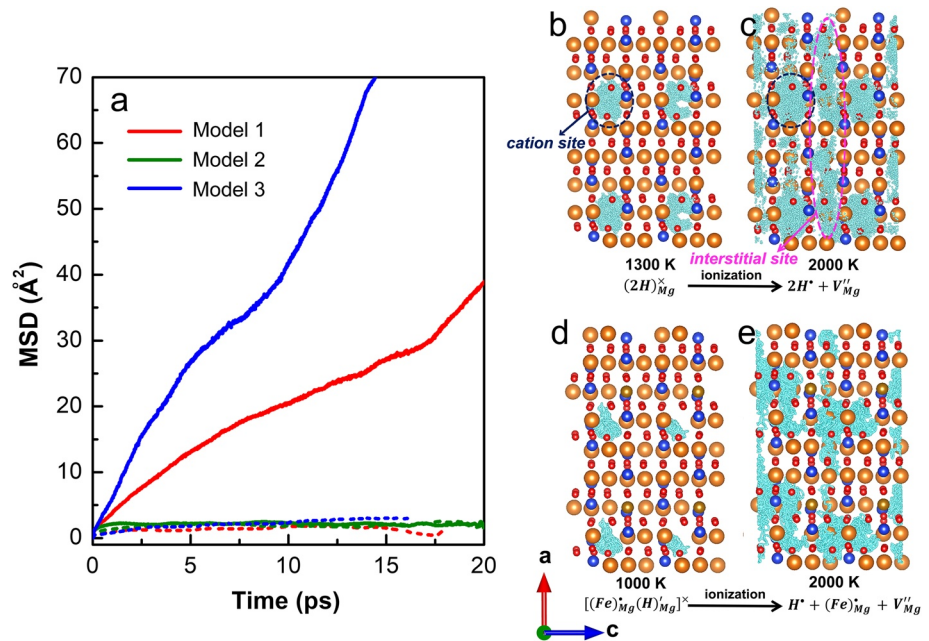


**Figure 1.** The mean square displacements (MSDs) and trajectories of protons in Model 1, Model 2, and Model 3 at different temperatures. (a) The dashed curves indicate the MSDs at low temperatures (1300 K for Model 1, Model 2, and 1000 K for Model 3). The solid curves indicate the MSDs at 2000 K. The increasing MSD as a function of simulation time indicates the obvious proton diffusion (red and blue solid curves). The trajectories of protons at Mg sites simulated at (a) 1,300 and (b) 2,000 K, and Fe sites simulated at (c) 1,000, and (d) 2,000 K. The cyan spheres are the trajectories of protons. Orange, blue, and red spheres represent Mg, Si, and O atoms in  $\text{Mg}_2\text{SiO}_4$  (olivine) crystalline. The dark blue and magenta dashed circles present cation and interstitial sites.

$$D = A \exp\left(-\frac{\Delta H}{kT}\right) \quad (8)$$

where  $\Delta H$  is the activation enthalpy,  $A$  is a pre-exponential factor,  $k$  is the Boltzmann constant, and  $T$  is the temperature. The electrical conductivity is calculated on the basis of the diffusion coefficients and the Nernst-Einstein equation (Equation 1).

Since a supercell is small (less than 506 atoms), water content is much higher than in any laboratory studies or in olivine in the mantle (water content  $\sim 0.01$ – $0.1$  wt%; e.g., [Peslier et al., 2017]). We used thermodynamic models of hydrogen-related defects (e.g., Karato, 2008) to extrapolate our results to compare with laboratory data or to apply to Earth's interior.

#### 4. Results

AIMD simulations were performed on Model 1, Model 2, and Model 3 at different temperatures to study the diffusion behavior of hydrogen. At low temperatures (1300 K for Model 1 and Model 2; 1000 K for Model 3), the hydrogen is trapped at the cation sites without appreciate diffusion in the crystal (Figure 1). At high temperatures, hydrogen escapes from the cation sites indicating a thermal ionization in Model 1 and Model 3 leading to the increase in MSD. In Model 2, hydrogen atoms at a Si vacancy site do not escape the vacancy site even at 2000 K, indicating a strong interaction between hydrogen and Si vacancy.

Once hydrogen is ionized from the Mg vacancy site, one has a proton at the interstitial site. The interstitial proton migrates fast with a high MSD. Notably, the migration of interstitial proton is highly anisotropic. The trajectories of interstitial protons are longer along the [100] direction compared to other directions (Figures 1d and 1e), indicating anisotropic proton diffusion. In order to understand the anisotropic diffusion behavior of protons in olivine, we conducted CINEB calculations to investigate the migration paths and barrier energies for protons in hydrous olivine along the [100], [010], and [001] directions. We found

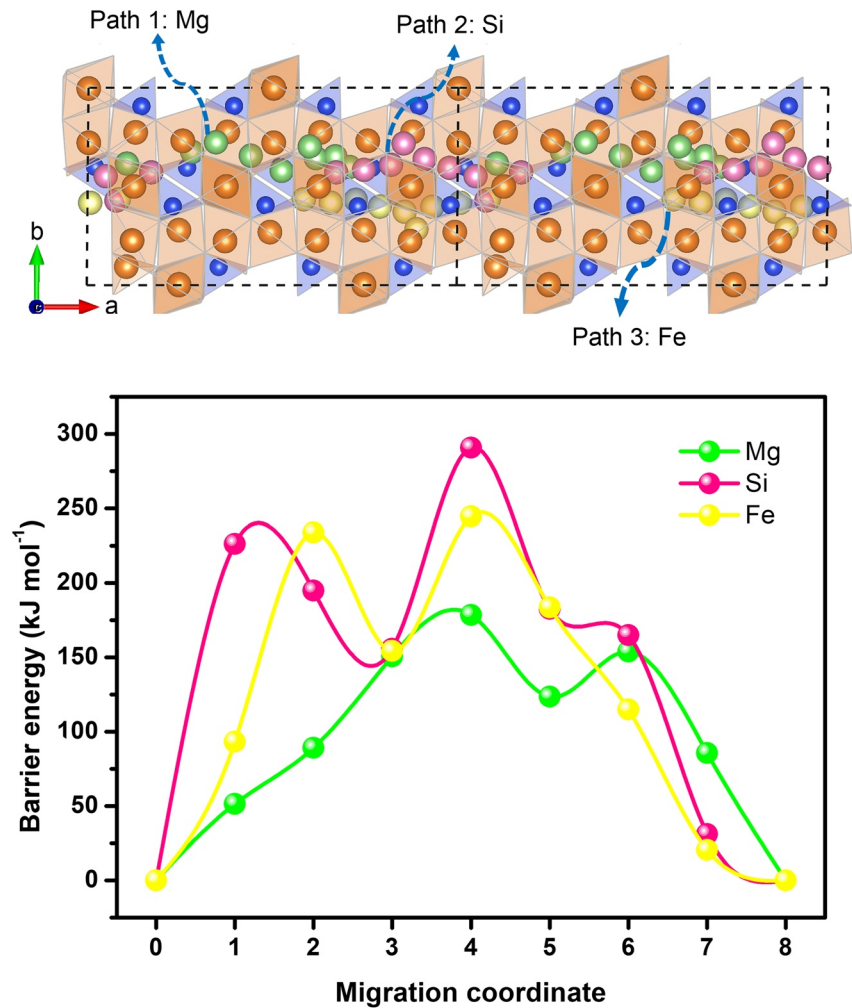


**Figure 2.** Proton migration paths and barrier energies along the [100] direction. In the crystalline of olivine, the green (path 1), pink (path 2), and yellow (path 3) spheres represent the [100] migration path for protons at Mg, Si vacancy and Fe sites corresponding to  $(2H)_{Mg}^{\times}$ ,  $(4H)_{Si}^{\times}$  and  $[(Fe)_{Mg}^{\bullet}(H)_{Mg}']^{\times}$  defects. The orange and blue polyhedrons are the  $MgO_6$  octahedrons and  $SiO_4$  tetrahedrons. The migration barrier energies for paths 1, 2, and 3 are shown with green squares, pink triangles, and yellow diamonds, respectively.

that the most favorable proton migration path for  $(2H)_{Mg}^{\times}$  and  $(4H)_{Si}^{\times}$  is along the [100] direction with barrier energies equal to 178.88 and 290.75  $\text{kJ mol}^{-1}$ . For the  $[(Fe)_{Mg}^{\bullet}(H)_{Mg}']^{\times}$  defect, the barrier energies along [100] and [010] are 244.23 and 203.85  $\text{kJ/mol}$  indicating weaker anisotropy (Figure 2). The barrier energies along other directions are shown in Table S2. The anisotropic proton diffusion behavior is consistent with the experimental results obtained by proton diffusion coefficient and conductivity measurements at high temperatures (Dai & Karato, 2014a; Du Frane & Tyburczy, 2012; Novella et al., 2017).

The water content in Model 1 and Model 3 is 16,330 and 7,938 ppm wt, respectively, which is larger than that of experimental samples and the asthenosphere condition. Protons interact strongly with other charged defects through the Coulombic force that depends on the mean distance of ions. Consequently, it is possible that high density of protons in our calculations might have an artifact on the mobility of protons and in such a case, the applications of our results to the cases with lower proton concentration (e.g., the asthenosphere) would be questionable.

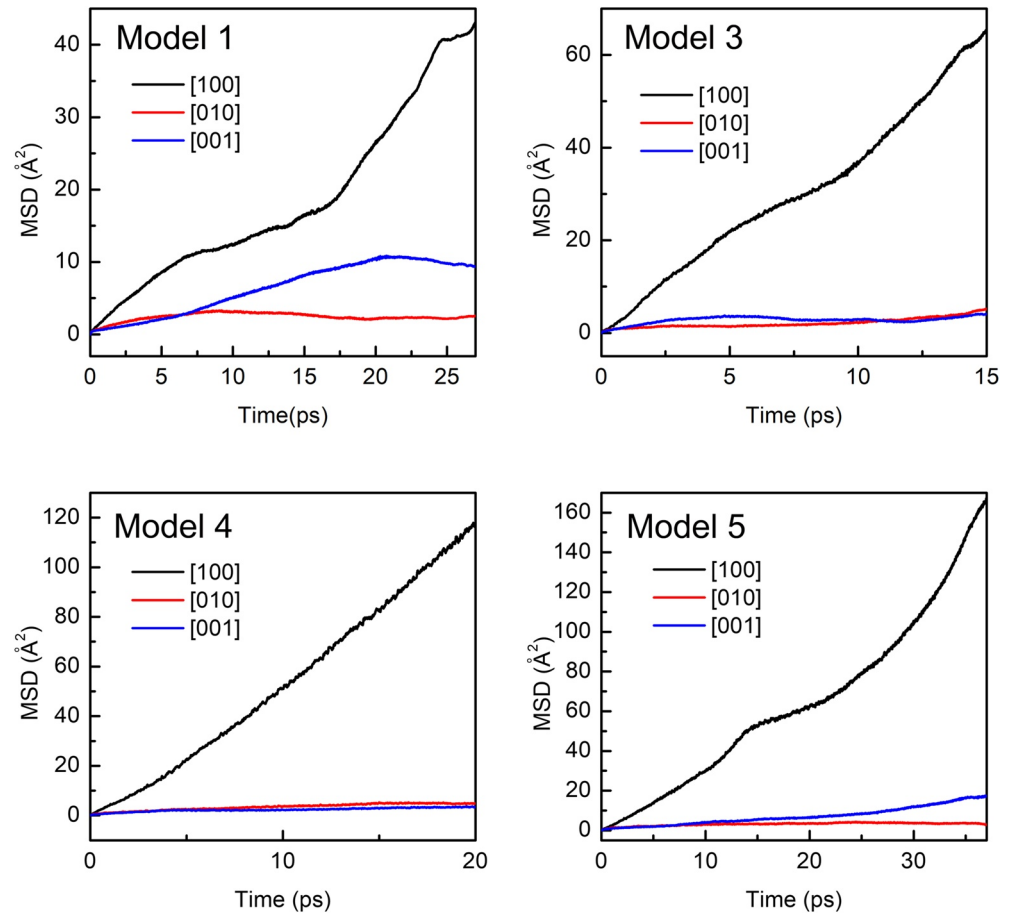


**Figure 3.** The mean square displacements (MSDs) of protons along the [100], [010], and [001] directions in Model 1, Model 3, Model 4, and Model 5 at 2000 K. The increasing of MSD along [100] is significantly higher than that of the other directions indicating profound anisotropic proton conductivity.

In order to examine the validity of extrapolation of these results to the case of lower water content ( $\sim 100$  ppm wt), we also performed calculations for larger supercells (Model 4-Model 9) with less water content. For Model 4 and Model 5, we also observed the diffusion rate of proton does not decrease due to less water content. We calculated the MSDs of protons along the [100], [010], and [001] directions at 2000 K (Figure 3). The MSDs along [100] were significantly larger than those along other directions, which confirms the anisotropic proton diffusion behavior in hydrous olivine at high temperature. However, we did not observe the ionization process of  $(2H)_{Mg}^{\times}$  in Model 6 (water content: 3,570 ppm wt) even at 2000 K (Figure 4). The reason for this behavior is discussed in the following section. We found Fe content also has an influence on the ionization process. In Fe-bearing Model 7 (water content: 3,488 ppm wt), the protons are ionized from  $V_{Mg}^{\prime}$  site and diffuse to a nearby Fe site. The Fe-bearing model (Model 7) shows a more notable increase in MSD compared to that of Model 6. It is likely that the presence of Fe atoms in olivine provides diffusion sites for protons and promotes their diffusion. It is also reported that the diffusion of protons can be promoted by hydrogen-polaron redox exchange (Kohlstedt & Mackwell, 1998; Mackwell & Kohlstedt, 1990) and protons diffuse faster in Fe-bearing olivine (Du Frane & Tyburczy, 2012; Novella et al., 2017). Therefore, we constructed Model 8 with about 10% Fe/(Fe + Mg) ratio. The MSD of Model 8 increases more rapidly than the MSDs of Model 6 and Model 7, and protons in Model 8 diffuse from one Fe site to another with the trajectory distributed along Fe sites (red circles in Figure 4).

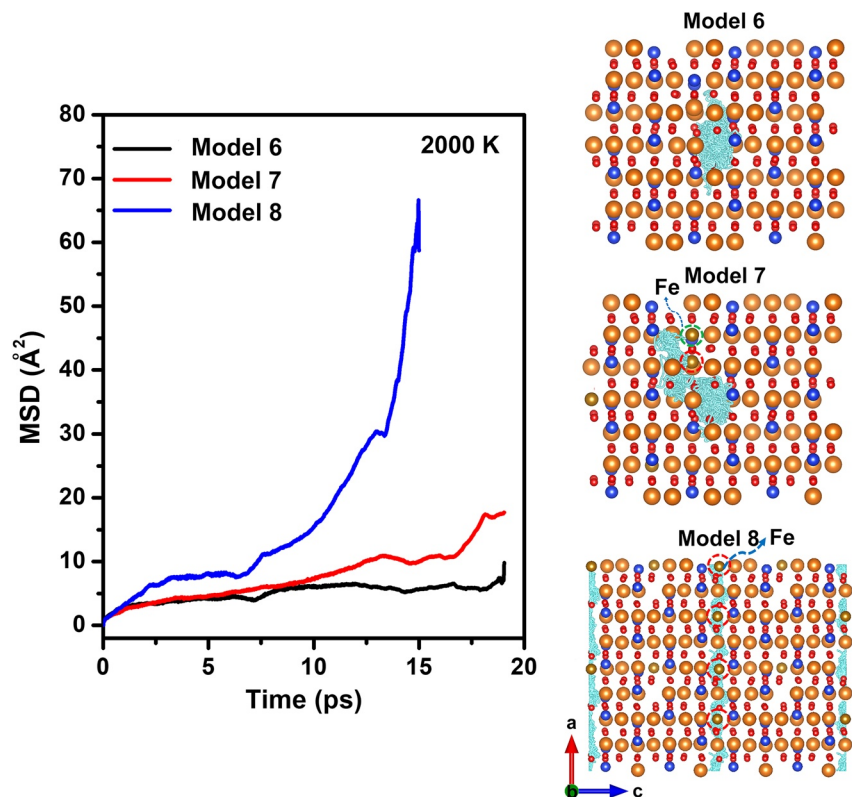


**Figure 4.** The mean square displacements (MSDs) and trajectories of protons in the Model 6, Model 7, and Model 8 at 2000 K. The cyan spheres are the trajectories of protons. Orange, brown, blue, and red spheres represent Mg, Fe, Si, and O atoms. The proton trajectory in Model 7 presents the diffusion of protons from  $V_{Mg}^{\prime}$  to a nearby Fe atom site. The diffusion of protons between different Fe sites is shown in Model 8. The Fe atoms in red and green dashed circle take the originate places of Mg and Si atoms, respectively.

## 5. Discussion

### 5.1. Proton Conduction Mechanism

Our results help understand how protons migrate in olivine that will shed some lights in interpreting the experimental results on proton-assisted electrical conductivity. We show the ionization effect of hydrogen dissolved in olivine cation sites: some fraction of hydrogen trapped as some defects such as  $(2H)_{Mg}^{\times}$  or  $(4H)_{Si}^{\times}$ , or  $\left[ (Fe)_{Mg}^{\bullet} (H)_{Mg}^{\prime} \right]^{\times}$  is ionized at high temperature. Ionized protons have high mobility to enhance electrical conductivity, and the conductivity is anisotropic due to the anisotropic ionization energy suggested by the CINEB calculations (Table S3). Verma and Karki (2009) also observed anisotropic migration barrier energies of protons in forsterite and wadsleyite. However, we also show that the degree of ionization differs among several types of hydrogen-defects. In addition, protons associated with Si defects are less mobile than the protons associated with Fe or Mg defects. This result is consistent with previous experimental study on the diffusion property of protons at different defects (Padrón-Navarta et al., 2014). Similarly, Caracas and Panero (2017) found that hydrogen atoms at Mg vacancies show higher diffusion rates compared to the hydrogen at Si sites in wadsleyite and ringwoodite.

In order to understand the proton diffusion mechanism in hydrous olivine with low water content, a CINEB calculation was undertaken on the proton migration within a supercell containing 506 atoms and found that the barrier energy remained unaltered with water content (black squares in Figure 5). In the case of Model 6, the two defects are far away from each other. Although a hydrogen atom can be activated to overcome the energy barrier, the most favorable location for the proton is still the nearby Mg vacancy due to the Coulomb



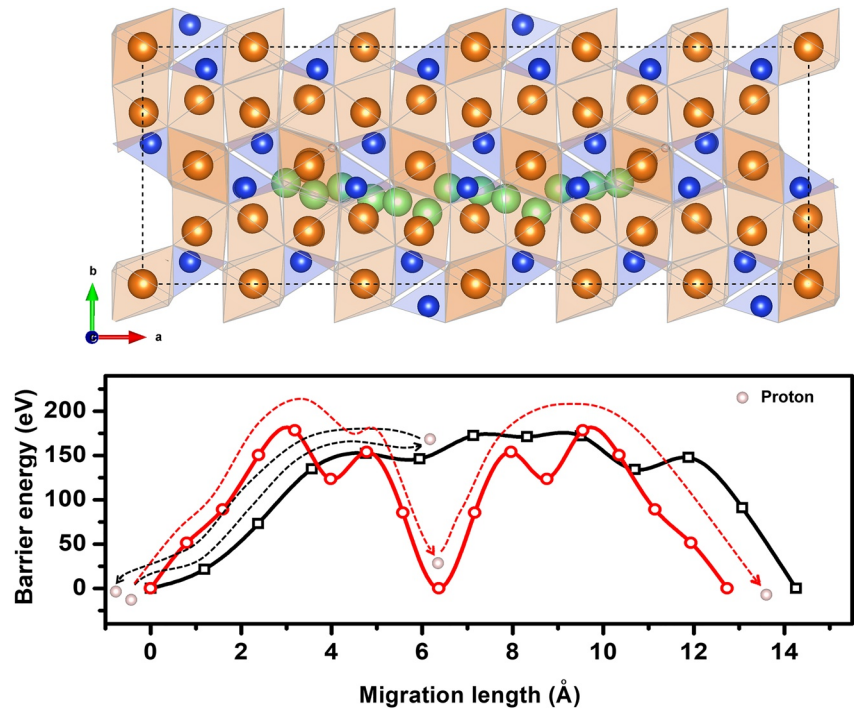
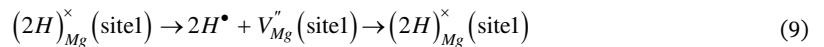
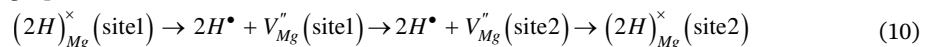


**Figure 5.** Proton migration paths and barrier energies along the [100] direction in Model 1 and Model 6 with different water content. The green spheres represent the [100] migration path of proton. The orange and blue polyhedrons are the  $\text{MgO}_6$  octahedrons and  $\text{SiO}_4$  tetrahedrons. The proton migration barrier energies and transport mechanism in hydrous olivine with different water content of 3,488 and 16,330 ppm wt are shown with black squares and red circles, respectively.

interaction. As a result, the proton will trace back to the initial position and couple with the Mg vacancy again. This process can be described by the black dashed curves in Figure 5 and the following equation,



For models with high water content (Model 1, Model 3, Model 4, and Model 5), thermally ionized protons can diffuse within the crystal by hopping between these defects (red circles in Figure 5). It should be noted that the defects for proton hopping do not have to be  $V_{Mg}^{\prime\prime}$ ; as observed in Model 7 and Model 8, Fe sites can also act as hopping sites during the hydrogen ionization and diffusion process. Thus, we propose an ionization-hopping mechanism for proton diffusion in hydrous olivine as shown in Figure 5 (red dashed curve) and the following equation,



The ionization process takes place at high temperature and generates interstitial protons. These interstitial protons diffuse through hopping sites in the lattice and contribute to electrical conductivity. Based on our simulations on Model 7 and Model 8,  $\text{Fe}^{2+}/\text{Fe}^{3+}$  redox can play the role of a hopping site in olivine and provide a network for proton diffusion when the Fe content is sufficient. This mechanism is verified in Model 9 that lower water content does not have a significant influence on the proton diffusion coefficient in Fe bearing hydrous olivine. In natural olivine, the hopping sites should also be abundant due to the presence of small polarons, Mg vacancies, and other defects such as  $\text{Mn}_{Mg}^{\times}$ ,  $\text{Cr}_{Mg}^{\bullet}$  and  $\text{Ti}_{Mg}^{\bullet\bullet}$  (Berry et al., 2005; Blanchard et al., 2017). In addition, increasing of cation Frenkel defects and significant  $\text{Mg}^{2+}$  and  $\text{Si}^{4+}$  diffusion at high temperature (e.g., Fei et al., 2018; Dohmen et al., 2002) may provide external diffusion paths and promote the ionization process of associated protons. Nevertheless, we did not observe this behavior due to the short simulation time in this study.

The concentration of protons is crucial for the conductivity and can be estimated by the Arrhenius equation:

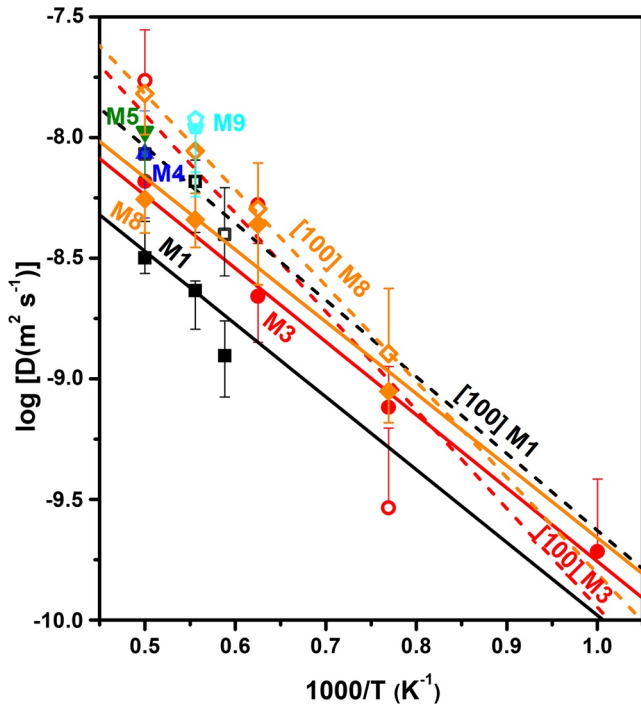


**Figure 6.** Calculated proton diffusion coefficients of different models at various temperatures. The diffusion coefficients of Model 1, Model 3, Model 4, Model 5, Model 8, and Model 9 (M1-M9) are denoted by black squares, red circles, blue triangles, green inverted triangles, orange diamonds, and cyan pentagons, respectively (solid symbols for total, and empty symbols for the [100] direction). The fitted data as a function of inverse temperature is plotted with solid curves (black, red, and orange for Model 1, Model 3, and Model 8), and dashed curves are the fitted proton diffusion coefficients along the [100] direction for Model 1, Model 3, and Model 8.

activation enthalpy for proton diffusion along the [100] direction in Model 1 and Model 3 are 178.85 and 244.23 kJ/mol, respectively, which is not very different from the experimental results obtained by conductivity ( $140 \pm 6$  kJ/mol) and diffusion coefficient ( $229 \pm 18$  kJ/mol) measurements (Dai & Karato, 2014a; Novella et al., 2017). However, we failed to obtain proton diffusion coefficients along the [010] and [001] directions due to the negligible proton diffusion along these directions in our models. The calculated migration barrier energies along other directions are also inconsistent with experimental results. It is true that the calculation on the migration barrier energy along unfavorable direction is inaccurate as an ion needs to pass through polyhedron sites in the lattice, which is quite unfavorable for ion migration. In addition, the diffusion of Mg, Si, and O defects at high temperature may assist proton diffusion along other directions.

Because all proton-enhanced conductivity and proton diffusion experiments were conducted in Fe-bearing olivine, we used our results on Fe-bearing olivine to compare with experimental results. We used the following equation to calculate electrical conductivity, and the contribution of small polaron and ionic ( $\text{Mg}^{2+}$ ) to the total conductivity are included in  $\sigma_{\text{dry}}$ .

$$\sigma_{\text{total}} = \sigma_{\text{dry}} + \sigma_{\text{proton}} \quad (13)$$

The total conductivities with different water content are plotted in Figure 7. It should be noted that the conductivities are estimated based on the hydrogen associated with  $V_{\text{Mg}}^{\times}$  or  $\text{Fe}^{3+}$  defects. The isotropic conductivity of hydrous olivine under asthenospheric conditions is crucial with potential implications on the conductivity anomaly structures. Based on our calculation results, approximately 80–160 ppm wt water content (associated with  $V_{\text{Mg}}^{\times}$  or  $\text{Fe}^{3+}$ ) in hydrous olivine is sufficient to generate the high conductivity

$$C_{p(a)} = C_{p(i)} + C_{p(\text{Mg})} \exp\left(-\frac{\Delta H_{\text{Mg}}}{kT}\right) + C_{p(\text{Fe})} \exp\left(-\frac{\Delta H_{\text{Fe}}}{kT}\right) + \dots \quad (11)$$

Here,  $C_{p(i)}$ ,  $C_{p(\text{Mg})}$ , and  $C_{p(\text{Fe})}$  represent proton concentrations at interstitial,  $V_{\text{Mg}}^{\times}$  and  $\text{Fe}_{\text{Mg}}^{\times}$  sites.  $\Delta H_{\text{Mg}}$  and  $\Delta H_{\text{Fe}}$  are the thermal activation enthalpies for protons at Mg and Fe defects. Hence, the total proton conductivity is expressed as:

$$\begin{aligned} \sigma = & \sigma_0 C_{p(i)} \exp\left(-\frac{\Delta H_I}{kT}\right) + \sigma_0 C_{p(\text{Mg})} \exp\left(-\frac{\Delta H_I - \Delta H_{\text{Mg}}}{kT}\right) \\ & + \sigma_0 C_{p(\text{Fe})} \exp\left(-\frac{\Delta H_I - \Delta H_{\text{Fe}}}{kT}\right) + \dots \quad (12) \end{aligned}$$

where  $\Delta H_I$  is the diffusion activation enthalpy of interstitial protons, and the diffusion activation enthalpy of hydrogen trapped at a cation site is  $\Delta H_I + \Delta H_M$ , where  $\Delta H_M$  is the enthalpy of thermal ionization ( $\Delta H_{\text{Mg}}$  or  $\Delta H_{\text{Fe}}$ ). Due to the thermal ionization effect, more interstitial protons are generated from cation defects at high temperatures, leading to the increase in proton conductivity.

## 5.2. Comparing Calculated Proton Conductivity With Experimental Results

We carried out more AIMD simulations for Model 1, Model 3, and Model 8 at different temperatures and calculated the proton diffusion coefficients and conductivities (Figures 2 & Figure 6). Hydrogen ionization in Model 1 and Model 3 becomes significant at temperatures above 1,600 and 1300 K, respectively. Protons in Model 1, Model 3, and Model 6 show similar activation enthalpies of  $\sim 57$  kJ/mol, which is much lower than the experimental results (Dai & Karato, 2014a; Novella et al., 2017). This is because the calculated activation enthalpies using AIMD do not include the enthalpies of thermal ionization ( $\Delta H_{\text{Mg}}$  and/or  $\Delta H_{\text{Fe}}$ ). The total activation enthalpy can be estimated by the barrier energy of proton migration calculated by CINEB (Ammann et al., 2010). Hence, the ac-

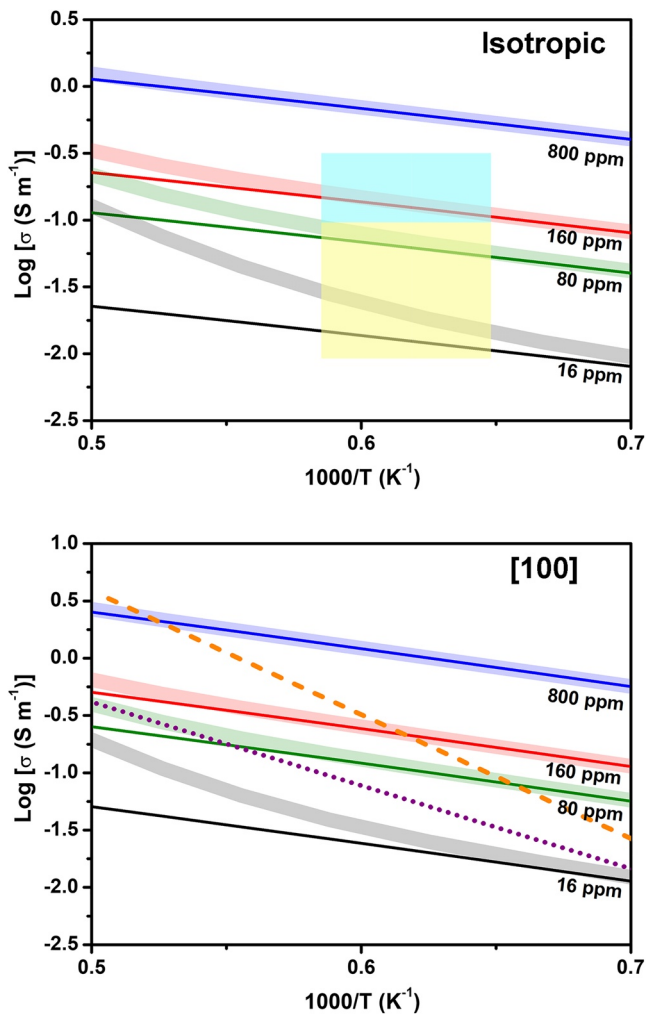


**Figure 7.** The extrapolated proton and total conductivities of Fe-bearing hydrous olivine as a function of inverse temperature and water content. The conductivities with 16, 80, 160, and 800 ppm wt water content associated with  $V_{\text{Mg}}^{\prime\prime}$  or  $\text{Fe}^{3+}$  are plotted with black, green, red, and blue curves. The thin-solid curves are the proton conductivities, and thick-light curves are the total conductivities counting on the measured conductivities of dry olivine (Gardés et al., 2014). The uncertainties of different measurements are within the thick curves. Upper and lower panels present the isotropic and anisotropic conductivities along the [100] direction, respectively. Light yellow area shows the conductivity range representing majority high-conductivity structures at the asthenosphere (Baba et al., 2006, 2010; Evans et al., 2005; Sarafian et al., 2015). Light cyan area represents the conductivity range of some ultra-high conductivity structures (Heinson et al., 2000; Naif et al., 2013). The dotted purple curve represents the measured conductivities of olivine with 80 ppm wt water (Dai & Karato, 2014a). The orange dashed curve represents the conductivities of olivine with 80 ppm wt water deduced from the measured proton diffusion coefficients (Novella et al., 2017).

anomaly ( $\sim 0.1 \text{ S m}^{-1}$ ). It suggests that the ionization effect is important in understanding the proton conductivity in hydrous olivine, and previous conductivity measurements at relatively low temperatures ignored the contribution of ionized hydrogen from cation sites, hence their extrapolated data underestimates the proton conductivity of hydrous olivine under the conditions of the asthenosphere.

Our models show more conspicuous anisotropic conductivities than those of the experimental results. This can be attributed to the limitation of the numbers and kinds of proton defects in our simulation models. Therefore, only the anisotropic conductivities along the [100] direction are compared with experimental results (Dai & Karato, 2014a; Novella et al., 2017). As the ionization behavior becomes significant at high temperatures, the comparison of specific conductivity values is mainly restricted to the temperature condition of the asthenosphere (1,550–1700 K). The comparison suggests anisotropic conductivities along the [100] direction can be understood by the hydrogen ionization effect. The difference between experimental and computational data is within half an order of magnitude, which may be caused by the different pressures and kinds of hydrous defect in the samples.

In our simulations, the conductivities are estimated based on the hydrogen associated with  $V_{\text{Mg}}^{\prime\prime}$  or  $\text{Fe}^{3+}$  defects, which ionizes at high temperature and increases the proton conductivity. On the contrary,  $(4H)_{\text{Si}}^{\times}$  defect is very stable even at  $\sim 2000 \text{ K}$ . Considering the presence of  $(4H)_{\text{Si}}^{\times}$  defects in hydrous olivine (e.g., Padrón-Navarta & Hermann, 2017; Tollan et al., 2017; Walker et al., 2007; Xue et al., 2017), the proton conductivity in a natural sample should be lower than our prediction. The concentration of  $(4H)_{\text{Si}}^{\times}$ , which is critical in governing the conductivity of hydrous olivine, is strongly dependent on the temperature and pre-anneal silica activity (Le Losq et al., 2019). Thus, the sample synthesis method and conditions may also have a significant influence on the conductivity of hydrous olivine. Our calculated quantities are higher than the measured conductivities (Dai & Karato, 2014a), which may suggest the presence of hydrogen trapped at Si vacancies in these natural samples. Generally, our study indicates the conductivity of hydrous olivine strongly depends on the hydrogen site (associated with  $V_{\text{Mg}}^{\prime\prime}$  and/or  $V_{\text{Si}}^{\prime\prime}$ ). As the hydrogen concentration at  $V_{\text{Mg}}^{\prime\prime}$  is not well constrained in the asthenosphere, it is difficult to compare the calculated conductivity with the asthenosphere conductivity.

## 6. Conclusions

Hydrogen associated with different cation defects present different mobility. Using AIMD simulations, the thermal ionization process of hydrogen at Mg and Fe defects is observed under the asthenosphere conditions, while hydrogen is trapped at Si vacancy even at 2000 K. The ionized hydrogen can be transported to a nearby hopping defect through interstitial sites.  $\text{Fe}^{2+}$  in hydrous olivine acts as hopping defects, and  $\sim 10\%$  Fe/(Fe + Mg) content is sufficient to form a network for proton conduction.

The ionization effect increases the concentration of protons and enhances the electrical conductivity of hydrous olivine at high temperature. Moreover, the diffusion of ionized hydrogen is highly anisotropic resulting in anisotropic conductivity along the [100] direction. Our results are consistent with previous experiments conducted at relative high temperatures.

## Conflict of Interest

The authors declare no conflicts of interest relevant to this study.

## Data Availability Statement

Additional computational method and detailed data sets for this research are included in the Supporting Information S1. Numerical computations were performed on Hefei advanced computing center. The data is available in 4TU Center for Research Data (<https://doi.org/10.4121/13250774.v1>).

## Acknowledgments

This study was supported by the Strategic Priority Research Program (B) of the Chinese Academy of Sciences (XDB 18010401). The authors also acknowledge the support of the National Natural Science Foundation of China (41774101, 42074104), the Youth Innovation Promotion Association of CAS (2020394), and by the National Science Foundation of USA (EAR-1764271). The manuscript was written through contributions of all authors. All authors have given approval to the final version of the manuscript. Numerical computations were performed on Hefei advanced computing center. We thank the anonymous reviewers and the editors for their constructive review and comments.

## References

- Alfè, D., & Gillan, M. J. (1998). First-principles calculation of transport coefficients. *Physical Review Letters*, *81*, 1561. <https://doi.org/10.1103/physrevlett.81.5161>
- Ammann, M. W., Brodholt, J. P., Wookey, J., & Dobson, D. P. (2010). First-principles constraints on diffusion in lower-mantle minerals and a weak D" layer. *Nature*, *465*, 462–465. <https://doi.org/10.1038/nature09052>
- Anderson, O. L., & Suzuki, I. (1983). Anharmonicity of three minerals at high temperature: Forsterite, fayalite, and periclase. *Journal of Geophysical Research*, *88*, 3549–3556. <https://doi.org/10.1029/jb088ib04p03549>
- Baba, K., Chave, A. D., Evans, R. L., Hirth, G., & Mackie, R. L. (2006). Mantle dynamics beneath the East Pacific Rise at 17°S: Insights from the mantle electromagnetic and tomography (MELT) experiment. *Journal of Geophysical Research*, *111*, B02101. <https://doi.org/10.1029/2004JB003598>
- Baba, K., Utada, H., Goto, T. N., Kasaya, T., Shimizu, H., & Tada, N. (2010). Electrical conductivity imaging of the Philippine Sea upper mantle using seafloor magnetotelluric data. *Physics of the Earth and Planetary Interiors*, *183*, 44–62. <https://doi.org/10.1016/j.pepi.2010.09.010>
- Belonoshko, A. B., Rosengren, A., Burakovsky, L., Preston, D. L., & Johansson, B. (2009). Melting of Fe and Fe<sub>0.9375Si0.0625</sub> at Earth's core pressures studied using ab initio molecular dynamics. *Physical Review B: Condensed Matter*, *79*, 220102. <https://doi.org/10.1103/physrevb.79.220102>
- Berry, A. J., Hermann, J., O'Neill, H. S. C., & Foran, G. J. (2005). Fingerprinting the water site in mantle olivine. *Geology*, *33*, 869–872. <https://doi.org/10.1130/g21759.1>
- Blanchard, M., Ingrin, J., Balan, E., Kovács, I., & Withers, A. C. (2017). Effect of iron and trivalent cations on OH defects in olivine. *American Mineralogist*, *102*, 302–311. <https://doi.org/10.2138/am-2017-5777>
- Brodholt, J. P., & Refson, K. (2000). An ab initio study of hydrogen in forsterite and a possible mechanism for hydrolytic weakening. *Journal of Geophysical Research*, *105*. <https://doi.org/10.1029/2000jb900057>
- Caracas, R., & Panero, W. R. (2017). Hydrogen mobility in transition zone silicates. *Progress in Earth and Planetary Sciences*, *4*, 9. <https://doi.org/10.1186/s40645-017-0119-8>
- Dai, L., & Karato, S. (2014a). High and highly anisotropic electrical conductivity of the asthenosphere due to hydrogen diffusion in olivine. *Earth and Planetary Science Letters*, *408*, 79–86. <https://doi.org/10.1016/j.epsl.2014.10.003>
- Dai, L., & Karato, S. (2014b). The effect of pressure on the electrical conductivity of olivine under the hydrogen-rich conditions. *Physics of the Earth and Planetary Interiors*, *232*, 51–56. <https://doi.org/10.1016/j.pepi.2014.03.010>
- Dohmen, R., Chakraborty, S., & Becker, H.-W. (2002). Si and O diffusion in olivine and implications for characterizing plastic flow in the mantle. *Geophysical Research Letters*, *29*, 2030. <https://doi.org/10.1029/2002gl015480>
- Downs, R. T., Zha, C., Duffy, T. S., & Finger, L. W. (1996). The equation of state of forsterite to 17.2 GPa and effects of pressure media. *American Mineralogist*, *96*, 1039–1053. <https://doi.org/10.2138/am-1996-1-207>
- Du Frane, W. L., & Tyburczy, J. A. (2012). Deuterium–hydrogen interdiffusion in olivine: Implications for point defects and electrical conductivity. *Geochemistry, Geophysics, Geosystems*, *13*, Q03004. <https://doi.org/10.1029/2011GC003895>
- Evans, R. L., Hirth, G., Baba, K., Forsyth, D., Chave, A., & Mackie, R. (2005). Geophysical evidence from the MELT area for compositional controls on oceanic plates. *Nature*, *437*, 249–252. <https://doi.org/10.1038/nature04014>
- Fei, H., Druzhbin, D., & Katsura, T. (2020). The Effect of water on ionic conductivity in olivine. *Journal of Geophysical Research: Solid Earth and Planets*, *125*, e2019JB019313. <https://doi.org/10.1029/2019JB019313>
- Fei, H., Koizumi, S., Sakamoto, N., Hashiguchi, M., Yurimoto, H., Marquardt, K., et al. (2018). Mg lattice diffusion in iron-free olivine and implications to conductivity anomaly in the oceanic asthenosphere. *Earth and Planetary Science Letters*, *484*, 204–212. <https://doi.org/10.1016/j.epsl.2017.12.020>
- Gardés, E., Gaillard, F., & Tarits, P. (2014). Toward a unified hydrous olivine electrical conductivity law. *Geochemistry, Geophysics, Geosystems*, *15*, 4984–5000. <https://doi.org/10.1002/2014gc005496>
- Guyot, F., Wang, Y., Gillet, P., & Ricard, Y. (1996). Quasi-harmonic computations of thermodynamic parameters of olivines at high-pressure and high-temperature. A comparison with experiment data. *Physics of the Earth and Planetary Interiors*, *98*, 17–29. [https://doi.org/10.1016/s0031-9201\(96\)03174-3](https://doi.org/10.1016/s0031-9201(96)03174-3)
- He, Y., Sun, S., & Li, H. (2021). Ab initio molecular dynamics investigation of the elastic properties of superionic Li<sub>2</sub>O under high temperature and pressure. *Physical Review B: Condensed Matter*, *103*, 174105. <https://doi.org/10.1103/physrevb.103.174105>
- Heinson, G., Constable, S., & White, A. (2000). Episodic melt transport at mid-ocean ridges inferred from magnetotelluric sounding. *Geophysical Research Letters*, *27*, 2317–2320. <https://doi.org/10.1029/2000gl011473>
- Henkelman, G., Uberuaga, B. P., & Jonsson, H. (2000). A climbing image nudged elastic band method for finding saddle points and minimum energy paths. *The Journal of Chemical Physics*, *113*, 9901–9904. <https://doi.org/10.1063/1.1329672>
- Karato, S. (1990). The role of hydrogen in the electrical conductivity of the upper mantle. *Nature*, *347*, 272–273. <https://doi.org/10.1038/347272a0>
- Karato, S. (2008). *Deformation of earth materials: Introduction to the rheology of the solid earth*: Cambridge University Press.
- Karato, S. (2013). Theory of isotope diffusion in a material with multiple species and its implications for hydrogen-enhanced electrical conductivity in olivine. *Physics of the Earth and Planetary Interiors*, *219*, 49–54. <https://doi.org/10.1016/j.pepi.2013.03.001>

- Karato, S. (2015). Some notes on hydrogen-related point defects and their role in the isotope exchange and electrical conductivity in olivine. *Physics of the Earth and Planetary Interiors*, 248, 94–98. <https://doi.org/10.1016/j.pepi.2015.08.007>
- Karato, S. (2019). Some remarks on hydrogen-assisted electrical conductivity in olivine and other minerals. *Progress in Earth and Planetary Sciences*, 6, 55. <https://doi.org/10.1186/s40645-019-0301-2>
- Karato, S., & Wang, D. (2013). Electrical conductivity of minerals and rocks. In S. Karato (Ed.), *Physics and chemistry of the deep Earth* (pp. 145–182). New York: Wiley-Blackwell. <https://doi.org/10.1002/9781118529492.ch5>
- Kohlstedt, D. L., & Mackwell, S. J. (1998). Diffusion of hydrogen and intrinsic point defects in olivine. *Zeitschrift für Physikalische Chemie*, 207, 147–162. [https://doi.org/10.1524/zpch.1998.207.part\\_1\\_2.147](https://doi.org/10.1524/zpch.1998.207.part_1_2.147)
- Kohn, W., & Sham, L. J. (1965). Self-consistent equations including exchange and correlation effects. *Physical Review A*, 140, 1133–1138. <https://doi.org/10.1103/physrev.140.a1133>
- Kresse, G., & Furthmüller, J. (1996). Efficient iterative schemes for ab initio total-energy calculations using a plane-wave basis set. *Physical Review B: Condensed Matter*, 54(16), 11169. <https://doi.org/10.1103/physrevb.54.11169>
- Le Losq, C., Jollands-Tollan, M. C. P. M. E., Hawkins, R., Ginsberg, S. B., & O'Neill, H. S. (2019). Point defect populations of forsterite revealed by two-stage metastable hydroxylation experiments. *Contributions to Mineralogy and Petrology*, 174, 53. <https://doi.org/10.1007/s00410-019-1590-6>
- Mackwell, S. J., & Kohlstedt, D. L. (1990). Diffusion of Hydrogen in Olivine: Implications for Water in the Mantle. *Journal of Geophysical Research*, 95, 5079–5088. <https://doi.org/10.1029/jb095ib04p05079>
- Mookherjee, M., Stixrude, L., & Karki, B. (2008). Hydrous silicate melt at high pressure. *Nature*, 452, 983–986. <https://doi.org/10.1038/nature06918>
- Naif, S., Key, K., Constable, S., & Evans, R. L. (2013). Melt-rich channel observed at the lithosphere–asthenosphere boundary. *Nature*, 495, 356–359. <https://doi.org/10.1038/nature11939>
- Novella, D., Jacobsen, B., Weber, P. K., Tyburczy, J. A., Ryerson, F. J., & Du Frane, W. L. (2017). Hydrogen self-diffusion in single crystal olivine and electrical conductivity of the Earth's mantle. *Scientific Reports*, 7, 5344. <https://doi.org/10.1038/s41598-017-05113-6>
- Padrón-Navarta, J. A., & Hermann, J. (2017). A Subsolidus Olivine Water Solubility Equation for the Earth's Upper Mantle. *Journal of Geophysical Research: Solid Earth and Planets*, 122, 9862–9880. <https://doi.org/10.1002/2017jb014510>
- Padrón-Navarta, J. A., Hermann, J., & O'Neill, H. S. (2014). Site-specific hydrogen diffusion rates in forsterite. *Earth and Planetary Science Letters*, 392, 100–112. <https://doi.org/10.1016/j.epsl.2014.01.055>
- Perdew, J. P., & Zunger, A. (1981). Self-interaction correction to density functional approximations for many-electron systems. *Physical Review B: Condensed Matter*, 23, 5048–5079. <https://doi.org/10.1103/physrevb.23.5048>
- Peslier, A. H., Schönbächler, M., Busemann, H., & Karato, S. (2017). Water in the Earth's interior: Distribution and origin. *Space Science Reviews*, 212, 743–810. <https://doi.org/10.1007/s11214-017-0387-z>
- Poe, B., Romano, C., Nestola, F., & Smyth, J. R. (2010). Electrical conductivity anisotropy of dry and hydrous olivine at 8 GPa. *Physics of the Earth and Planetary Interiors*, 181, 103–111. <https://doi.org/10.1016/j.pepi.2010.05.003>
- Pommier, A., Kohlstedt, D. L., Hansen, L. N., Mackwell, S., Tasaka, M., Heidelberg, F., & Leinenweber, K. (2018). Transport properties of olivine grain boundaries from electrical conductivity experiments. *Contributions to Mineralogy and Petrology*, 173, 41. <https://doi.org/10.1007/s00410-018-1468-z>
- Sarafian, E., Evans, R. L., Collins, J. A., Elsenbeck, J., Gaetani, G. A., Gaherty, J. B., et al. (2015). The electrical structure of the central Pacific upper mantle constrained by the NoMelt experiment. *Geochemistry, Geophysics, Geosystems*, 16, 1115–1132. <https://doi.org/10.1002/2014GC005709>
- Sifré, D., Gardés, E., Massuyeau, M., Hashin, L., Hier-Majumder, S., & Gaillard, F. (2014). Electric conductivity during incipient melting in the oceanic low-velocity zone. *Nature*, 509, 81–85. <https://doi.org/10.1038/nature13245>
- Sun, W., Yoshino, T., Kuroda, M., Sakamoto, N., & Yurimoto, H. (2019). H-D interdiffusion in single-crystal olivine: Implications for electrical conductivity in the upper mantle. *Journal of Geophysical Research: Solid Earth and Planets*, 124, 5696–5707. <https://doi.org/10.1029/2019jb017576>
- Tollan, P. M. E., Smith, R., O'Neill, H. S., & Hermann, J. (2017). The responses of the four main substitution mechanisms of H in olivine to H<sub>2</sub>O activity at 1050°C and 3 GPa. *Progress in Earth and Planetary Sciences*, 4, 14. <https://doi.org/10.1186/s40645-017-0128-7>
- Umemoto, K., Wentzcovitch, R. M., Hirschmann, M. M., Kohlstedt, D. L., & Withers, A. C. (2011). A first-principles investigation of hydrous defects and IR frequencies in forsterite: The case for Si vacancies. *American Mineralogist*, 96, 1475–1479. <https://doi.org/10.2138/am.2011.3720>
- Verma, A. K., & Karki, B. B. (2009). Ab initio investigations of native and protonic point defects in Mg<sub>2</sub>SiO<sub>4</sub> polymorphs under high pressure. *Earth and Planetary Science Letters*, 285, 140–149. <https://doi.org/10.1016/j.epsl.2009.06.009>
- Walker, A. M., Hermann, J., Berry, A. J., & O'Neill, H. S. C. (2007). Three watersites in upper mantle olivine and the role of titanium in the water weakening mechanism. *Journal of Geophysical Research: Solid Earth and Planets*, 112, B05211. <https://doi.org/10.1029/2006jb004620>
- Wang, D. J., Mookherjee, M., Xu, Y. S., & Karato, S. I. (2006). The effect of water on the electrical conductivity of olivine. *Nature*, 443, 977–980. <https://doi.org/10.1038/nature05256>
- Withers, A. C., Hirschmann, M. M., & Tenner, T. J. (2011). The effect of Fe on olivine H<sub>2</sub>O storage capacity: Consequences for H<sub>2</sub>O in the martian mantle. *American Mineralogist*, 96, 1039–1053. <https://doi.org/10.2138/am.2011.3669>
- Xue, X., Kanzaki, M., Turner, D., & Loroch, D. (2017). Hydrogen incorporation mechanisms in forsterite: New insights from 1H and 29Si NMR spectroscopy and first-principles calculation. *American Mineralogist*, 102, 519–536. <https://doi.org/10.2138/am-2017-5878>
- Yang, X. (2012). Orientation-related electrical conductivity of hydrous olivine, clinopyroxene and plagioclase and implications for the structure of the lower continental crust and uppermost mantle. *Earth and Planetary Science Letters*, 317/318, 241–250. <https://doi.org/10.1016/j.epsl.2011.11.011>
- Yoshino, T., Matsuzaki, T., Yamashita, S., & Katsura, T. (2006). Hydrous olivine unable to account for conductivity anomaly at the top of the asthenosphere. *Nature*, 443, 973–976. <https://doi.org/10.1038/nature05223>
- Yoshino, T., Yamazaki, D., & Mibe, K. (2009). Well-wetted olivine grain boundaries in partial molten peridotite in the asthenosphere. *Earth and Planetary Science Letters*, 283, 167–173. <https://doi.org/10.1016/j.epsl.2009.04.007>
- Zhao, Y., Ginsberg, S. B., & Kohlstedt, D. L. (2004). Solubility of hydrogen in olivine: Dependence on temperature and iron content. *Contributions to Mineralogy and Petrology*, 147, 155–161. <https://doi.org/10.1007/s00410-003-0524-4>